Journal of Materials Chemistry A

Defective by design: Vanadium-substituted iron oxide nanoarchitectures as cation-insertion hosts for electrochemical charge storage

Journal:	*Journal of Materials Chemistry A*
Manuscript ID:	TA-ART-02-2015-001507.R1
Article Type:	Paper
Date Submitted by the Author:	27-Apr-2015
Complete List of Authors:	Chervin, Christopher; U.S. Naval Research Laboratory, Code 6170 Ko, Jesse; University of California at Los Angeles, Miller, Bryan; U.S. Naval Research Laboratory, Dudek, Lisa; University of California at Los Angeles, Mansour, Azzam; Naval Surface Warfare Center, Donakowski, Martin; U.S. Naval Research Laboratory, Brintlinger, Todd; Naval Research Laboratory, Materials Science and Technology Gogotsi, Pavel; U.S. Naval Research Laboratory, Chattopadhyay, Soma; Elgin Community College, Shibata, Tomohiro; Elgin Community College, Parker, Joseph; U.S. Naval Research Laboratory, Hahn, Benjamin; U.S. Naval Research Laboratory, Rolison, Debra; Naval Research Laboratory, Code 6170 Long, Jeffrey; U.S. Naval Research Laboratory, Surface Chemistry Branch

Defective by design: Vanadium-substituted iron oxide nanoarchitectures as cation-insertion hosts for electrochemical charge storage

Christopher N. Chervin,*[a] Jesse S. Ko,[b] Bryan W. Miller,[a] Lisa Dudek,[c] Azzam N. Mansour,[d] Martin D. Donakowski,[a] Todd Brintlinger,[e] Pavel Gogotsi,[a] Soma Chattopadhyay,[f,g] Tomohiro Shibata,[g] Joseph F. Parker,[a] Benjamin P. Hahn,[a] Debra R. Rolison,[a] and Jeffrey W. Long*[a]

[a] U. S. Naval Research Laboratory, Surface Chemistry Branch (Code 6170), Washington, D.C. 20375, USA

[b] Department of Materials Science and Engineering, University of California at Los Angeles (UCLA), Los Angeles, California 90095, USA

[c] Department of Chemistry and Biochemistry, University of California at Los Angeles (UCLA), Los Angeles, California 90095, USA

[d] Naval Surface Warfare Center, Carderock Division, Materials and Power Systems Branch (Code 6160), West Bethesda, MD, 20817, USA

[e] U. S. Naval Research Laboratory, Materials and Sensors Branch (Code 6360), Washington, D.C. 20375, USA

[f] Physical Sciences Department, Elgin Community College, 1700 Spartan Drive, Elgin, IL 60123.

[g] Previously at: Sector 10 ID, CSRRI- IIT, Advanced Photon Source, 9700 S . Cass Avenue, Lemont, IL 60439.

*Corresponding authors: christopher.chervin@nrl.navy.mil (C. N. Chervin); jeffrey.long@nrl.navy.mil (J. W. Long)

Received (in XXX, XXX) Xth XXXXXXXXX 20XX, Accepted Xth XXXXXXXXX 20XX
DOI: 10.1039/b000000x

Vanadium-substituted iron oxide aerogels (2:1 Fe:V ratio; VFe_2O_x) are synthesized using an epoxide-initiated sol–gel method to form high surface-area, mesoporous materials in which the degree of crystallinity and concentration of defects are tuned via thermal treatments under controlled atmospheres. Thermal processing of the X-ray amorphous, as-synthesized VFe_2O_x aerogels at 300 °C under O_2-rich conditions removes residual organic byproducts while maintaining a highly defective γ-Fe_2O_3–like local structure with minimal long-range order and vanadium in the +5 state. When as-synthesized VFe_2O_x aerogels are heated under low partial pressure of O_2 (*e.g.*, flowing argon), a fraction of vanadium sites are reduced to the +4 state, driving crystallization to a Fe_3O_4–like cubic phase. Subsequent thermal oxidation of this nanocrystalline VFe_2O_x aerogel re-oxidizes vanadium +4 to +5, creating additional cation vacancies and re-introducing disordered oxide domains. We correlate the electrochemical charge-storage properties of this series of VFe_2O_x aerogels with their degree of order and chemical state, as verified by X-ray diffraction, X-ray photoelectron spectroscopy, and X-ray absorption spectroscopy. We find that the disordered O_2-heated VFe_2O_x aerogel yields the highest Li^+- and Na^+-insertion capacities among this series, approaching 130 mA h g^{-1} and 70 mA h g^{-1}, respectively. Direct heat-treatment of the VFe_2O_x aerogel in flowing argon to yield the partially reduced, nanocrystalline form results in significantly lower Li^+-insertion capacity (77 mA h g^{-1}), which improves to 105 mA h g^{-1} by thermal oxidation to create additional vacancies and structural disorder.

Introduction

High-performance materials used as positive electrodes for rechargeable Li-ion batteries often contain expensive, toxic, and/or strategic metals (in the form of pure or mixed-metal oxides such as $LiCoO_2$), driving the search for less expensive, nontoxic alternatives. One such example is $LiFePO_4$, which offers a thermodynamically favorable Li^+-insertion potential of ~3.5 V *vs*. Li and a high reversible capacity (160 mA h g^{-1}), in conjunction with the cost and environmental benefits inherent to iron-based materials.[1] Certain iron oxides (FeO_x), particularly those that have cation-defective structures, also exhibit promise as positive electrode materials. For example, maghemite (γ-Fe_2O_3, more accurately denoted as $Fe^{3+}_{2.67}\square_{0.33}O_4$) is a cation-deficient spinel phase that inserts Li^+ into structural cation vacancies at more positive potentials than observed in the defect-free analogue, magnetite (Fe_3O_4).[2,3,4,5]

The cation-vacancy population of the γ-Fe_2O_3 structure can be further increased by substituting a fraction of the Fe^{3+} sites with metal cations of higher oxidation state, such as Mo^{6+} or V^{5+}.[6,7] We recently reported that a nanocrystalline Mo-substituted ferrite ($Mo_{0.59}Fe_{1.50}\square_{0.91}O_4 \cdot nH_2O$) provides >4× improvement in specific capacity for Li^+-insertion relative to an analogous γ-Fe_2O_3 material.[8,9] The population of electrochemically active defects in metal oxides can also be amplified when these materials are expressed in nanoscale forms,[10] ranging from hollow nanospheres[11,12] to three-dimensionally (3D) ultraporous nanoarchitectures such as aerogels.[13] Aerogels exhibit high specific surface areas (100–600 m^2 g^{-1}) that encourage surface-sited defect formation, while providing other structural characteristics beneficial to electrochemical functionality: (*i*) through-connected, covalently bonded networks of nanometric particles that electrically wire the electrode architecture; (*ii*) through-connected networks of mesopores and/or macropores that enable efficient diffusion and transport of molecules and ions; and (*iii*) nanoscale domains that minimize the solid-state diffusion distance for ion insertion.

Previous investigations of V_2O_5 aerogels as Li^+-insertion hosts illustrate how the aerogel framework can enhance electrochemical performance.[13,14,15,16] For example, while microcrystalline V_2O_5 only intercalates ~2 Li^+ per formula unit,[17] V_2O_5 aerogels insert >4 Li^+ per formula unit (chemically or electrochemically).[13,18,19] Spectroelectrochemical analysis of Li^+-insertion into V_2O_5 aerogels implies that beyond 2 Li^+ per V_2O_5, the increase in Li^+ content may not occur by traditional insertion mechanisms but rather by processes at accessible defect sites that are not accompanied by a change in the oxidation state of vanadium.[20]

Herein, we combine these two materials design strategies to produce deliberately defective cation-insertion hosts based on V-substitution into a γ-Fe_2O_3–like structure that is expressed as an ultraporous, high surface-area aerogel. Vanadium-substituted iron oxide (2:1 Fe:V ratio; VFe_2O*x*) aerogels are achieved using an epoxide-driven sol–gel synthesis[21,22,23,24] that yields amorphous oxides of the desired stoichiometry, but whose crystallinity and defective nature can be tuned by subsequent thermal processing under controlled atmospheres. We explore the cation-insertion properties of VFe_2O*x* aerogels as a function of crystalline order, V and Fe oxidation state, and surface area/porosity. Direct thermal processing under flowing O_2 at 300 °C produces X-ray-amorphous VFe_2O*x* aerogels that exhibit reversible Li^+- and Na^+-insertion specific capacities approaching 130 mA h g^{-1} and 70 mA h g^{-1}, respectively, a result of high specific surface area (231 m^2 g^{-1}), a defective γ-Fe_2O_3 local structure, and V present in the +5 oxidation state. The local and long-range atomic structures and the chemical state of the VFe_2O*x* aerogels as a function of thermal treatment were elucidated by X-ray absorption spectroscopy, X-ray diffraction, and X-ray photoelectron spectroscopy; material morphology and composition were examined by electron microscopy and energy-dispersive spectroscopy.

Experimental

VFe_2O*x* aerogel synthesis and processing

The VFe_2O*x* aerogels were synthesized by adapting the alkoxide-precursor, epoxide-initiated sol–gel method[25] using an Fe-to-V ratio of 2:1. The use of vanadium salts rather than an alkoxide precursor led to precipitates rather than gels. In a typical synthesis, $FeCl_3 \cdot 6H_2O$ (3.0846 g; 97%, Sigma-Aldrich) was dissolved in 10 mL of ethanol (200 proof, Warner-Graham Company) via sonication and then chilled in an aqueous ice bath. In a second container, vanadium triisopropoxide (1.3832 g; 96%, Alfa Aesar; stored in a refrigerator at 35 °C before use) was added drop-wise into 20 mL of ethanol pre-chilled in an aqueous ice bath. The vanadium solution was equilibrated for a few minutes and then chilled to –78 °C in a dry ice–ethanol bath. The two chilled solutions were combined with an additional 10 mL rinse with ethanol to ensure quantitative transfer of the Fe^{3+}; the V-Fe solution was equilibrated for ~3 min in the dry ice–ethanol bath. Next, 12 mL of propylene oxide (Sigma-Aldrich 99%; passed through a column of activated alumina and stored in a refrigerator at 35 °C before use) was quickly added to the container and the solution was covered with Parafilm™. The solution was equilibrated for

~5 min in the –78 °C bath and then placed in an aqueous ice bath and stirred for ~45 min, during which time the solution changed from translucent orange to dark reddish-brown. The sol was removed to ambient temperature and gelation occurred within 10 min. The gel was aged overnight with the Parafilm™ seal maintained; the mother liquor within the gel pores was then exchanged with several 200-mL aliquots of ethanol over a 24-h period to remove reaction byproducts, followed by several days of solvent exchange with 200-mL aliquots of acetone (certified ACS; Fisher Scientific).

The acetone-exchanged gels were transferred under excess acetone into a supercritical drier (Polaron, Quorum Technologies), and solvent-exchanged with liquid CO_2 at 10 °C. The CO_2 was then taken to 44 °C and 9 MPa, well beyond its supercritical point of 31 °C and 7.4 MPa, before the pressure was released. For comparison, unsubstituted FeO*x* aerogels were prepared by the epoxide method using the $FeCl_3 \bullet 6H_2O$ precursor, ethanol solvent, and propylene oxide gel-initiator as described above (*i.e.*, the same molar ratio of cations to epoxide and cation to solvent), but carried out under ambient temperature (~20 °C).

The as-synthesized VFe_2O*x* and FeO*x* aerogels were calcined to 300 °C in alumina boats within a calibrated tube furnace (MTI Corporation OTF-1200X) under flowing Ar or O_2 at ~50 $cm^3\ min^{-1}$ with heating and cooling ramp rates of 1 °C min^{-1} and 4-h dwell times at the calcining temperature. Samples heated under high and low partial pressure of oxygen (p_{O_2}) are referred to as 300-O_2 and 300-Ar, respectively. The samples designated as 300-Ar-O_2 were first subjected to a low p_{O_2} heat treatment, cooled to room temperature and then heated under high p_{O_2} using the same temperature, ramp rate, and dwell time.

Materials characterization

Surface areas and pore-size distributions of the VFe_2O*x* and FeO*x* aerogels were measured using nitrogen physisorption (Micromeritics ASAP 2020 porosimeter). All samples were degassed at 80 °C for 12 h, backfilled with N_2 at room temperature, and then immediately placed on the instrument for characterization. Surface area was determined from the linear portion of the adsorption isotherm using the model of Brunauer–Emmet–Teller. Pore size distributions were calculated from the entire adsorption isotherm data using Micromeritics DFTPlus software (DFT model for a cylindrical geometry and Halsey curve thickness).

Aerogel morphology was imaged using scanning electron microscopy (SEM; Carl Zeiss Leo

Supra 55 microscope operating at 5 keV) and transmission electron microscopy (TEM; JEOL JEM 2200FS microscope operating at 200 kV). Elemental analysis was made with the SEM using energy dispersive spectroscopy (EDS; operating at 20 keV). For SEM measurements, the aerogel powders were mounted onto aluminum SEM stubs using double-sided carbon tape; for TEM measurements, the powders were ground in isopropanol and drop cast onto lacey carbon substrates.

The temperatures necessary for crystallization and volatilization of synthesis byproducts as a function of calcining atmosphere were characterized using simultaneous thermoanalytical and calormetric measurements with a Netzsch STA 449 F1 Jupiter thermogravimetric analyzer (TGA/DSC). Approximately 10 mg of as-synthesized aerogel was placed in an alumina crucible and equilibrated under the desired atmosphere for ~1 h before heating. The samples were heated to 550 °C at 10 °C min^{-1} in either Ar or O_2.

Powder X-ray diffraction (PXRD) profiles were collected on a Rigaku SmartLab X-ray diffractometer with a fixed CuKα radiation (λ = 1.5406 Å). Scans were recorded from 20 to 80°2θ, with a 0.02° step size and an integration time of 1 s per step. For materials where the PXRD indicated crystallinity, average crystallite sizes were calculated from the peak indexed to the (400) peak of the magnetite crystal structure; we chose the (400) reflection because it is intense and sufficiently isolated to avoid peak overlap from other reflections. Synchrotron PXRD data for 300-Ar and 300-Ar-O_2 VFe_2O_x aerogels were collected at beamline 11-BM at the Advanced Photon Source at Argonne National Laboratory (λ = 0.413851 Å). The data were refined with the General Structure Analysis System (GSAS) with EXPGUI;[26,27] models of maghemite ($P4_32_12$ ICDS #87121) and magnetite (Fd-3m, ICDS #20596) and assuming the stoichiometry for the aerogel was $Fe_{8x/(8+\square)}V_{(24-8x)/(8+\square)}\square_{3\square/(8+\square)}O_4$ ($x \approx 2$).

X-Ray Photoelectron Spectroscopy (XPS) was used to examine the chemical state and relative concentrations of Fe, V, and O using a Thermo Scientific K-Alpha X-ray photoelectron spectrometer at a chamber pressure $<5.0\times10^{-8}$ torr and equipped with a monochromatic Al Kα source (1486.68 eV) using a 400-μm elliptical spot size. The VFe_2O_x aerogel specimens were packed into wells of the powder module sample holder. The spectra were obtained at an energy step-size of 0.15 eV by averaging 25 scans of the Fe *2p*, V *2p*, O *1s*, C *1s*, and Cl *2p* regions (the Cl region was examined to ensure >99% conversion/removal of chloride). The spectra were analyzed with Avantage® software version 5.35 using a Shirley-derived background subtraction

model and peak-shifting relative to the adventitious C*1s* peak of 284.6 eV. The V$2p_{3/2}$ peaks were fitted with a floating Gaussian–Lorentzian ratio.

Room-temperature V and Fe K-edge X-ray absorption spectra of VFe_2O_x and FeO_x aerogels for as-synthesized materials and following heat treatments were collected in transmission mode at beamline 10-ID-B at the Advanced Photon Source at Argonne National Laboratory. The samples were prepared by attaching the powders to scotch tape and then folding several layers of the powder-tape assembly together; a method that gives reasonable results for homogenized powders such as aerogel materials. The energy scale was calibrated with respect to the first inflection point energies of the Fe and V foil standards at 7112.0 and 5465.0 eV, respectively. The pre-edge background was determined from a linear fit to the energy range of –150 to –30 eV relative to the edge energy. The normalization step was determined from a cubic polynomial fit over the energy range 150 to ~800 eV relative to the edge energy. The half-height energy was used to define the wave number k = 0. The background for the extended X-ray absorption fine structure (EXAFS) was determined using cubic spline procedures over the range 2–12 $Å^{-1}$ with the FT range set to 3–11 Å with k^3-weighted EXAFS spectra and a Hanning window of 1.0 $Å^{-1}$. The XAFS data analysis was carried out using the IFEFFIT suite of programs (Athena and Artemis).[28,29]

Electrode preparation

Aluminum foil current collectors (Alfa Aesar; either 0.5-mm thick, 99.9% metals basis or 0.13-mm thick, 99.9995% metals basis) for three-electrode and coin-cell configurations were prepared by sanding one side of the foil with 120-grit sand paper and then alkaline-etching in 1 M NaOH at ambient temperature for 20 min, rinsing with deionized water, and acid-etching at 80°C in 1 M HCl. The etched foils were rinsed with deionized water and air-dried at 100°C overnight. The current collectors for three-electrode half-cell configurations were 0.5-mm thick and cut into 2 cm × 1 cm pieces, whereas the foils for coin-cells were 0.13-mm thick and cut into ½”-diameter disks.

Active cathode material inks were prepared by making a slurry in N-methyl-2-pyrrolidone (NMP; 99.5% anhydrous, Sigma-Aldrich) of 85% active material, 8% Super P carbon black (source) and 7% polyvinylidene fluoride binder (PVdF; Kynar® HSV 900). Approximately 15–20 mg of active material powder was combined with carbon in a mortar and pestle and ground

for ~3 min to ensure that the powders were well-mixed to which a 5% PVdF solution in NMP was added and the wet mixture ground for 15 min. As necessary, NMP was added drop-wise to maintain a consistency of warm honey. The slurry was applied to the current collector with a spatula and then air dried for ~1 h followed by vacuum drying overnight at 120 °C. After drying, the electrodes were sandwiched between two weigh papers and pressed at 5000 psi and then immediately weighed and pumped into an Ar atmosphere glove box. For the half-cell electrodes, the slurries were painted onto a 1 cm × 1 cm area of the aluminum current collector, whereas for the coin-cell disks, the entire ½" face was painted with the slurry. The mass of active material was calculated as 85% of the weight of the applied film, as determined by the mass difference of the aluminum substrate before and after applying, drying, and pressing the film.

Electrochemical characterization

Cyclic voltammetric measurements were made with a Solartron SI1286 Electrochemical Interface using a three-electrode configuration in an Ar atmosphere glove box. For Li^+-insertion experiments an electrolyte of 1 M $LiPF_6$ in 1:1:1 ethylene carbonate:diethyl carbonate:dimethyl carbonate (BASF) was used and the reference and auxiliary electrodes were made from Li foils (250-µm thick). The Na^+-insertion experiments were made with Na-foil auxiliary and reference electrodes in an electrolyte comprising 1 M $NaClO_4$ in propylene carbonate (99.7% anhydrous, Sigma-Aldrich), which was prepared in an Ar atmosphere glove box and dried with molecular sieves (3 Å, Sigma-Aldrich) before use. The cathodes were cycled between 2.0 and 4.0 V *vs.* Li/Li^+ or 1.7 and 3.7 V *vs.* Na/Na^+ from 0.5 to 50 mV s^{-1}. The specific capacity was determined by averaging the integrated anodic and cathodic currents and normalizing to the mass of active material on the film.

Coin-cell measurements were performed in CR 2032 coin cells (MTI corporation) that consisted of (working outward from anode side) a Teflon®-separated negative electrode can, a stainless-steel spring, two stainless-steel spacers with a 250-µm–diameter Li-foil disc attached to the second spacer, two 2400 Celgard separators, the cathode film deposited on aluminum-foil current collector as described above, and a positive electrode can. The cells were assembled in an Ar-filled glove box. The cathode and the Celgard separator were infiltrated with the $LiPF_6$ electrolyte at 20 mm(Hg) for 4 h in the glove box antechamber and excess electrolyte was applied to the Li anode during cell assembly. The coin-cell cycling was controlled with an Arbin

BT2000 cycler, in the range of 2 V to 4 V at 10 mA g^{-1} of active material, starting with an initial charge step.

Results and Discussion

Synthesis of VFe_2O_x aerogels

The VFe_2O_x aerogels were synthesized using sol–gel protocols in which a proton-scavenging epoxide (propylene oxide) drives hydrolysis and condensation of metal(aquo-hydroxy) complexes to form metal-oxide gel networks; subsequent supercritical CO_2 extraction of the liquid-filled gels produces monolithic aerogels.[21] Epoxide-based sol–gel chemistry is a versatile route to synthesize iron oxides[21,22,23,24] as well as other transition metal and rare-earth oxides (e.g., Y_2O_3-stabilized ZrO_2, $La_{0.85}Sr_{0.15}MnO_3$, $NiCo_2O_4$, $La_{9.33}Si_6O_{26}$, and $Gd_{0.1}Ce_{0.9}O_2$).[25,30,31,32,33,34] Hydrated metal chlorides are the most common precursors due to their high solubility in alcohols and water, and because chloride anions act on the protonated epoxide via nucleophilic attack to shift the equilibrium of the hydrolysis/condensation reactions. Iron(III) chlorides behave ideally for epoxide-based sol–gel methods,[35] but vanadium(III) chloride precursors hydrolyze too rapidly, preferentially forming precipitates rather than stable gels. We adapted our prior strategy for bimetallic oxide gels in which one of the metals was introduced as an alkoxide,[25] and used vanadium tri-isopropoxide ($V(^iOPr)_3$), a well-known precursor for synthesizing V_2O_5 aerogels.[36] While more stable than vanadium chloride, $V(^iOPr)_3$ is still hydrolytically sensitive under ambient conditions, thus our sol–gel reactions were performed at reduced temperatures (dry ice–ethanol bath, –72 °C). In the present case, propylene oxide is added to an ethanolic solution of $V(^iOPr)_3$ and Fe(III) chloride, resulting in robust VFe_2O_x gels that are ultimately processed into high surface-area, ultraporous aerogels.

Characterization of VFe_2O_x aerogel structure and composition

The as-synthesized VFe_2O_x aerogels comprise interpenetrating networks of through-connected solid and pores with feature sizes on the order of tens of nanometers, typical for aerogel-type materials (Fig. 1 and Fig. S1). The porous, nanostructured nature of this material is confirmed by N_2-sorption porosimetry, which shows specific surface area of 535 $m^2 g^{-1}$, cumulative pore volume of 1.6 $cm^3 g^{-1}$ (Table 1), and a wide distribution of pore sizes with an average of 13 nm (Fig. S2). As expected from a low-temperature sol–gel synthesis, the as-prepared VFe_2O_x aerogel is amorphous when examined by XRD.

The disordered, as-synthesized VFe_2O_x aerogel was subjected to thermal processing under controlled atmospheres to tune the crystallinity of the VFe_2O_x structure and to remove organic byproducts of the epoxide-driven reactions. Thermal analysis (simultaneous TGA and DSC) under flowing O_2 or Ar was performed to determine the lowest temperature necessary to transform and/or purify the as-synthesized VFe_2O_x aerogel (Fig. S3). Under either atmosphere the VFe_2O_x aerogel exhibits weight loss up to ~27%, mostly occurring before 300 °C; we attribute this weight loss to the volatilization of organic residues from the sol–gel synthesis.[31,37] On the basis of these findings, we chose 300 °C as our endpoint for thermal processing—a temperature sufficient to remove unwanted byproducts and to induce partial crystallization, but also mild enough to minimize particle ripening and concurrent loss of surface area. Following similar protocols reported earlier for FeO_x aerogels,[22] we also applied a two-stage treatment at 300 °C, first under Ar to induce crystallization and then under O_2 to oxidize the metal sites in the VFe_2O_x aerogels to obtain a more defective, γ-Fe_2O_3–like form. Elemental analysis of thermally processed VFe_2O_x aerogels by EDS confirms that the 2:1 Fe:V stoichiometry from the initial synthesis is retained.

Oxidative heat treatment of the as-synthesized VFe_2O_x aerogel partially densifies the networked structure while retaining the ultraporous morphology and broad pore-size distribution as determined by SEM, TEM, and N_2-porosimetry (Figs. 1, 2, and S2); total pore volume decreases ~20% to 1.3 $cm^3\,g^{-1}$ and the specific surface area is reduced to 231 $m^2\,g^{-1}$ (Table 1). Heat treatment under low p_{O_2} (300-Ar) also retains the ultraporous aerogel morphology (Figs. 2, S2, and S4) but further reduces surface area to 165 $m^2\,g^{-1}$ and pore volume to 0.95 $cm^3\,g^{-1}$ (Table 1). Subsequent oxidative heat treatment of the 300-Ar aerogel does not alter the pore-size distribution or surface area (Table 1 and Fig. S2). For comparison, a pure FeO_x aerogel calcined to 300 °C in O_2 has a higher surface area (416 $m^2\,g^{-1}$) and a narrower pore-size distribution centered at 38 nm, in contrast to the broad distribution of mesopores observed for all VFe_2O_x aerogels (Fig. S2).

The XRD-amorphous nature of the as-synthesized VFe_2O_x aerogel is retained with calcination in high p_{O_2} (300-O_2; Fig. 3), whereas heating to 300 °C under inert atmosphere (300-Ar) produces a nanocrystalline cubic phase with peaks corresponding to either maghemite (γ-Fe_2O_3; ICDD# 00-039-1346) or magnetite (Fe_3O_4; ICDD# 01-073-9877). Further oxidative heat treatment of the nanocrystalline 300-Ar VFe_2O_x aerogel induces a *decrease* in atomic order as evidenced by

broadened diffraction peaks, reduced peak intensity, and the appearance of a broad amorphous feature centered around 30°2θ (Fig. 3). Using Scherrer analysis of the (400) peak, the average crystallite sizes for the 300-Ar and 300-Ar-O_2 samples are calculated to be 9.2 and 7.9 nm, respectively. The average crystallite sizes are comparable to the distribution of primary particle sizes (5–15 nm) observed by TEM (Fig. 2); the slightly larger particle size derived from TEM is attributed to partial atomic disorder in the particles, which will not contribute to the average crystallite size. Although we established crystallinity of the VFe_2O*x* materials by XRD, the phase and degree of order in the VFe_2O*x* nanoarchitectures can also be qualitatively accessed by color and magnetic susceptibility. The amorphous aerogels (as-synthesized and 300-O_2–treated) are light brown and paramagnetic, whereas the nanocrystalline 300-Ar and 300-Ar-O_2 aerogels strongly interact with a permanent magnet and are black and dark brown, respectively.

The magnetite and maghemite spinel phases are isostructural and therefore difficult to differentiate, particularly in nanocrystalline materials where diffraction peaks broaden. To further elucidate the crystalline phase for the 300-Ar and 300-Ar-O_2 VFe_2O*x* aerogels, we used bright X-rays from a synchrotron source, combined with Rietveld analysis of the PXRD pattern (Fig. S5). We observe two phases in their diffraction profiles: (*i*) a nanocrystalline structure and (*ii*) an amorphous component (as evidenced by the presence of a large background despite the use of a synchrotron source). For Rietveld refinement, the ratio of Fe:V was fixed at 2:1 and it was assumed that vanadium occupy tetrahedral sites, as observed by Gillot and Nivoix for $V_xFe_{3-x}O_4$ phases where $x < 1$;[7] the amorphous component was accounted for with a ninth-order Chebyschev polynomial. When using the magnetite structure as a starting point, we obtain a better fit to the diffraction profile than when starting with the maghemite structure (see supporting information). We attribute the amorphous region at low 2θ to the disordered nature of aerogel surfaces and the large surface-to-bulk ratio present in these ultraporous oxide nanoarchitectures.

The relative diffraction peak intensities for (0,*k*,*l*) reflections are anomalously high for the 300-Ar VFe_2O*x* aerogel, as is the (0,4,4) peak intensity for the 300-Ar-O_2 aerogel. These anomalies indicate that stacking faults are present within the crystalline component although fitting a model of the stacking faults to the PXRD is inhibited by the amorphous contribution to the profile and nanocrystalline peak broadening.[38] This structure refines to a cubic unit cell with $a = 8.33$ Å and with coherent crystallite sizes of the 300-Ar and 300-Ar-O_2 samples calculated to be 9.50 and

7.53 nm, respectively, in good agreement with the Scherrer analysis of diffraction profiles from XRD.

The oxidation states of V and Fe in the VFe_2O_x aerogels were assessed by deconvolving XPS regional spectra for V*2p*$_{3/2}$ (Fig. 4) and Fe*2p*$_{3/2}$ (Fig. S6). The 300-O_2 aerogel had a single V*2p*$_{3/2}$ peak at 517.7 eV, which corresponds to V^{5+} state.[39] Spectra for the 300-Ar VFe_2O_x show two overlapping V*2p*$_{3/2}$ peaks at 517.2 and 516.1 eV that indicate a mixture of V^{5+} and V^{4+}, a result of partial reduction of V^{5+} sites during low-p_{O_2} heat treatment. Subsequent heating in O_2 (300-Ar-O_2) returns the vanadium to +5, as indicated by a single V*2p*$_{3/2}$ peak at 517.3 eV. The Fe*2p* regions for the three VFe_2O_x aerogels consist of broad peaks that generally do not differ between the various heat treatments. The position of the Fe*2p*$_{3/2}$ *satellite* suggests that the predominant oxidation state is Fe^{3+}, but the peak for 300-Ar has a slightly lower binding energy at 719.4 eV, which indicates the presence of Fe^{2+}.[40] The O*1s* spectra of all three samples are similar, and indicative of hydrated or defective oxides.

X-ray absorption spectroscopy was also performed on this series of VFe_2O_x aerogels, as well as analogous unsubstituted FeO_x aerogels, to determine oxidation state and local structure. The XANES region includes contributions from dipole-allowed transitions from *1s* states to unoccupied final states with *p* character (Figs. 5, S7, and S8). The pre-edge peak, however, is due to transitions from *1s* states to final states with *3d* character, which are forbidden by dipole selection rules but allowed by quadrupole selection rules. The intensity of quadrupole-allowed transitions is usually weaker than those of dipole-allowed transitions, as is the case for the Fe XANES (Figs. 5, S7, and S8).[41] For vanadium oxides, the intensity of the pre-edge peak is significantly enhanced due to lack of centrosymmetry as a result of the high degree of distortion of the VO_6 octahedral geometry. The X-ray edge energy (at half-height beyond the pre-edge peak) and the pre-edge peak energy display a positive shift with increase in V oxidation state.[42,43,44] The pre-edge peak intensity also increases with greater VO_6 octahedral distortion and to a lesser degree with increasing density of unoccupied *d* states that accompany higher V oxidation states.

The Fe oxidation state in the as-synthesized and 300-O_2 FeO_x aerogel is close to +3; thermal treatment under Ar shifts the Fe oxidation state to ~+2.8 (Fig. S7). The VFe_2O_x aerogel samples also have Fe oxidation states that remain within a narrow window very close to +3 (2.94–3.12), with the lowest Fe oxidation state exhibited by the 300-Ar aerogel (Fig. 5a and Fig. S8). In

agreement with XPS, the V K-edge XANES results indicate a +5 oxidation state for the as-synthesized VFe_2O_x aerogel and for the aerogels treated under oxidizing environments (300-O_2 and 300-Ar-O_2), whereas the heating under low p_{O_2} reduces the vanadium toward +4 (Fig. 5b and Fig. S8).[45] However, an increase in pre-edge peak intensity indicates a greater degree of distortion in the 300-Ar VFe_2O_x aerogel than that of the V^{4+} standard, VO_2.

The local structure of the as-synthesized FeO_x aerogel, as determined by EXAFS, is highly disordered, evidenced by a lack of significant contributions from higher coordination spheres in the region of the Fourier transform data above 2 Å (Fig. S9). Disorder decreases following calcination at 300 °C in O_2 as evidenced by the increase in the amplitude of the structure in the 2.2–3.6 Å region of the Fourier transform. Thermal treatment in Ar induces significant changes, particularly in the first coordination sphere (Fe–O peak centered at ~1.5 Å in the Fourier transforms data) of FeO_x, resulting in a local structure that is closely related to γ-Fe_2O_3 (maghemite), especially in the region dominated by Fe–Fe interactions (2.2–3.6 Å region). The shift in the Fe–O peak to slightly higher distance is consistent with the presence of a small fraction of Fe^{2+} as a result of heating in Ar. The local structure of Fe in VFe_2O_x is similar for the as-synthesized, 300-O_2, and 300-Ar-O_2 aerogels, and may be interpreted as a disordered form of γ-Fe_2O_3 (Fig. 6 and Fig. S10). The local structure of V for VFe_2O_x heated to 300 °C in Ar is clearly distinct from the structure that emerges under oxidative conditions (Fig. 6 and Fig. S11). The increase in the amplitudes of the structure in the 2.2–3.6 Å region of the Fourier transforms of the EXAFS spectra indicates that the 300-Ar VFe_2O_x aerogel exhibits a more ordered form related to γ-Fe_2O_3.

Based on the synchrotron PXRD, EXAFS, and TEM results, we posit that our material consists of domains of nanocrystalline magnetite-like and amorphous, maghemite-like oxide, similar to our previous assessment of FeO_x aerogels that showed mixed magnetite/maghemite character.[46] This broad, amorphous PXRD pattern has previously been observed for core–shell maghemite/magnetite FeO_x nanoparticles.[47]

Electrochemical cation-insertion as a function of structure and composition

We use these VFe_2O_x and FeO_x aerogels as model electrode materials with which to investigate the influence of structural order/disorder, cation-vacancy content, and V substitution on electrochemical charge-storage properties, focusing primarily on Li^+-insertion reactions in nonaqueous electrolytes. Cyclic voltammetry (CV) provides an initial assessment of capacity and

active potential window, as seen when VFe_2O_x or FeO_x aerogel powders are processed into conventional composite electrodes and cycled at 0.5 mV s^{-1} in a three-electrode cell (Fig. 7). In all cases, most of the capacity is delivered between 3.2 and 2.0 V *vs* Li, with broad voltammetric profiles reminiscent of pseudocapacitive processes.

Integration of the voltammograms to obtain capacity values shows that the 300-O_2 VFe_2O_x aerogel provides the highest specific capacity of the series, reaching 130 mA h g^{-1}. The impact of V substitution on electrochemical performance is clear when compared to an analogously processed FeO_x aerogel, which delivers only 60 mA h g^{-1}. The ideal stoichiometry for these respective oxides in their fully oxidized, cation-defective forms is $[Fe^{3+}_{8/3}\cdot\square_{1/3}]O_4$ and $[V^{5+}_{8/11}Fe^{3+}_{16/11}\cdot\square_{9/11}]O_4$, with greater vacancy content for V-substituted FeO_x due to the need for additional charge compensation when V^{5+} replaces Fe^{3+} in the spinel lattice. Assuming a 1:1 correlation between vacancy content and Li-ion capacity, and accounting for the difference in formula mass, VFe_2O_x should provide 2.90 times the specific capacity of an analogous cation-defective FeO_x material; experimentally, we observe capacity improves by a factor of 2.17.

Heating the as-synthesized VFe_2O_x aerogel directly in Ar produces a nanocrystalline and partially reduced form that exhibits much lower specific capacity (77 mA h g^{-1}) than the poorly crystalline, 300-O_2 aerogels. The diminished capacity expressed by 300-Ar VFe_2O_x is recovered by ~35% to 105 mA h g^{-1} after subsequent heating in O_2, which oxidizes all V to the +5 state and creates more cation vacancies, while also increasing overall structural disorder, all without altering specific surface area or pore structure. However, the fully oxidized, nanocrystalline 300-Ar-O_2 VFe_2O_x still does not achieve the Li-ion capacity of the X-ray-amorphous 300-O_2 analog. The difference in specific surface area (230 vs. 160 m^2 g^{-1}) for these two VFe_2O_x aerogels may play a role in establishing Li-ion capacity, as vacancies and defects are favored at surface sites. Similar trends are also observed for VFe_2O_x cycled in a Na-ion electrolyte, albeit achieving a lower total capacity due to the larger size of the Na^+ cation (Fig. 7); VFe_2O_x 300-O_2 yields 70 mA h g^{-1} in Na^+ electrolyte compared to 130 mA h g^{-1} in Li^+ electrolyte.

The oxygen-calcined, X-ray-amorphous VFe_2O_x aerogel was selected for galvanostatic cycling experiments (at 10 mA g^{-1}) in Li coin cells. Representative charge–discharge profiles are shown in Fig. 8a; the sloping nature of these curves is consistent with the broad shapes observed in the voltammetric tests. Capacity values were also derived from these galvanostatic experiments, returning 186 mA h g^{-1} and 157 mA h g^{-1} on first and second discharge, respectively; the capacity

drop in this case is likely due to solid electrolyte–interface (SEI) formation. Thereafter, capacity fades gently with specific capacity maintained at ~100 mA h g^{-1} through 50 cycles. Charge–discharge coulombic efficiency ranges between 87–89% over the 50 cycles examined, which may indicate parasitic side reactions occurring during charging or some incremental irreversibility in the Li^+-insertion process. Further work is underway to enhance cycling stability, understand SEI formation, and further amplify specific capacity in this new class of cation-insertion materials.

Conclusions

Using a combined strategy of cation-substitution and nanostructuring, we synthesize deliberately defective VFe_2O_x aerogels and demonstrate that increasing concentrations of cation vacancies concomitantly enhances their specific capacity for Li^+- and Na^+-insertion. Aerogel frameworks create a defect-rich structure with high accessibility to the defect sites, and the substitution of tetrahedral iron sites with V^{5+} induces further vacancy formation. We observe the highest specific capacity (130 mA h g^{-1}) in Li^+-containing electrolyte when the VFe_2O_x aerogel is calcined in oxidizing atmospheres such that high surface area is retained and the X-ray amorphous oxide expresses γ-Fe_2O_3–like local structure.

Acknowledgements

This work was supported by the U. S. Office of Naval Research. Use of the Advanced Photon Source at Argonne National Laboratory was supported by the U. S. Department of Energy, Office of Science, Office of Basic Energy Sciences, under Contract No. DE-AC02-06CH11357. M.D.D. and B.P.H. were NRC–NRL postdoctoral associates.

TABLE 1: Brunauer–Emmett–Teller (BET) surface areas, Barrett–Joyner–Halenda (BJH) pore volumes, and specific discharge capacities for select VFe_2O_x and FeO_x aerogels

Sample	BET surface area ($m^2\ g^{-1}$)[a]	BJH pore volume ($cm^3\ g^{-1}$)	discharge capacity in Li^+-electrolyte (mA h g^{-1})[b]
VFe_2O_x as-synthesized	535	1.6	n/a
VFe_2O_x 300-O_2	231	1.3	130
VFe_2O_x 300-Ar	165	0.95	77
VFe_2O_x 300-Ar-O_2	156	0.87	105
FeO_x 300-O_2	416	2.3	60

[a] Values are ± 2% for replicate analyses within batch and ± 10% for batch-to-batch analysis

[b.] Capacities derived by integration of voltammetric curves at 0.5 mV s^{-1} scan rate.

Figure 1

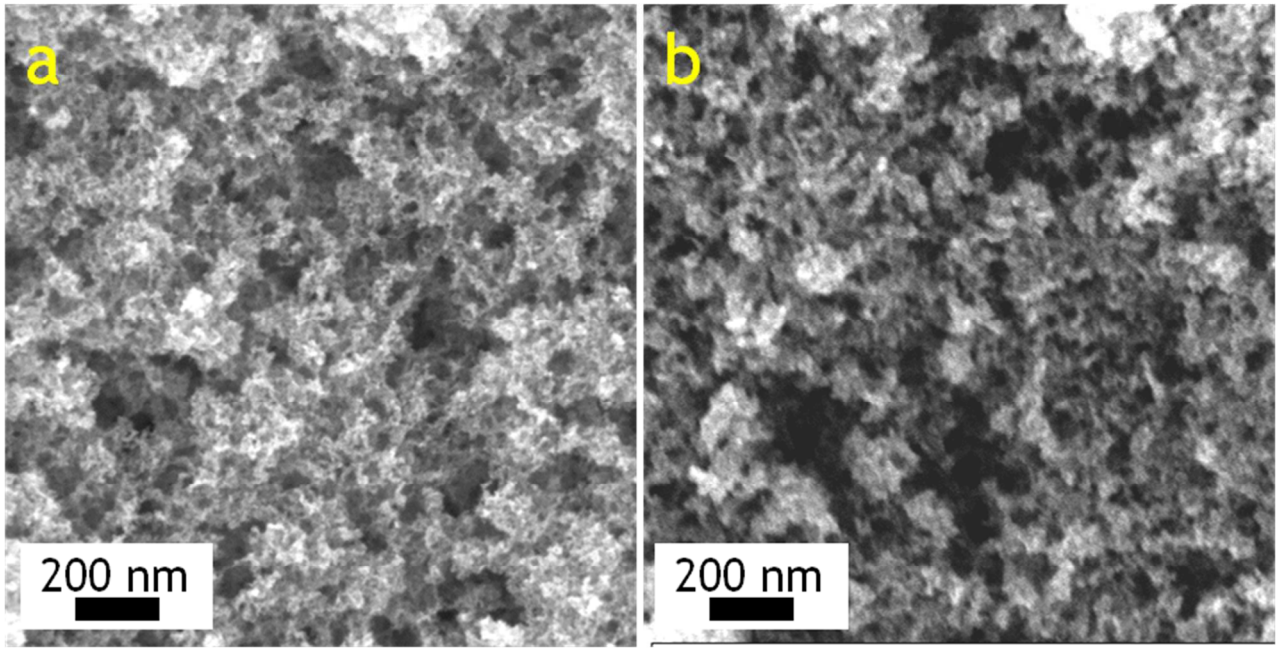

Fig 1 Scanning electron micrographs of VFe_2Ox aerogels: (a) as-synthesized an (b) 300-O_2.

Figure 2

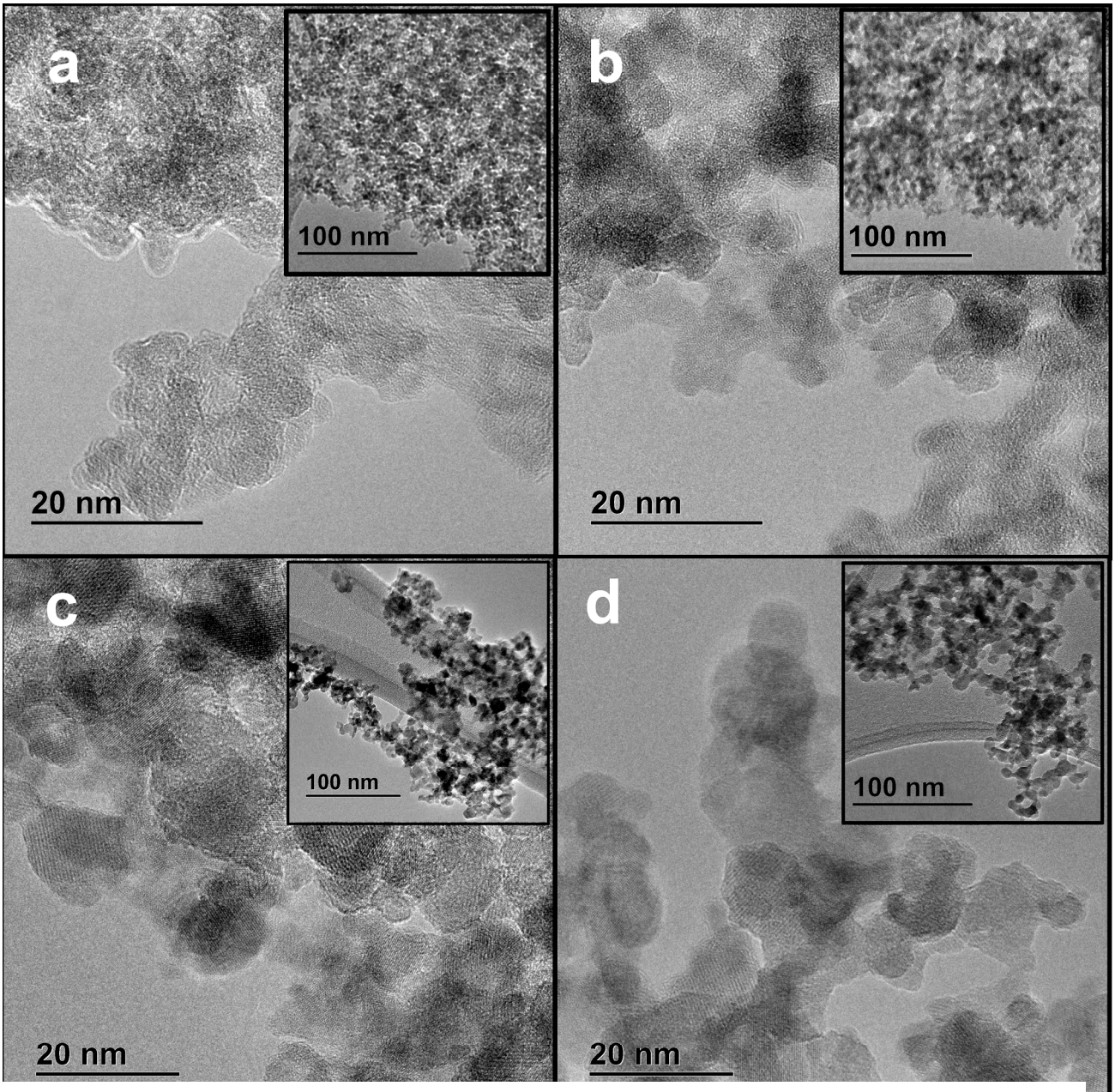

Fig 2 Transmission electron micrographs of VFe_2Ox aerogels: (a) as-synthesized, (b) 300-O_2, (c) 300-Ar, and (d) 300-Ar-O_2.

Figure 3

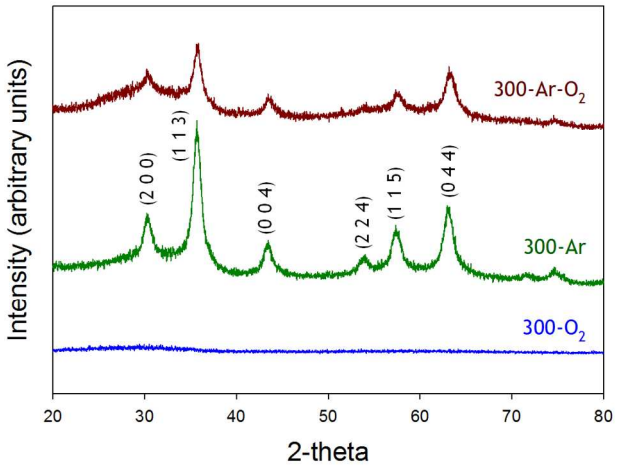

Fig 3 X-ray diffraction profiles of VFe_2Ox aerogels: 300-O_2 (—), 300-Ar (—), and 300-Ar-O_2 (—). Diffraction peaks for 300-Ar and 300-Ar-O_2 index to either maghemite (γ-Fe_2O_3; ICDD# 00-039-1346) or magnetite (Fe_3O_4; ICDD# 01-073-9877).

Figure 4

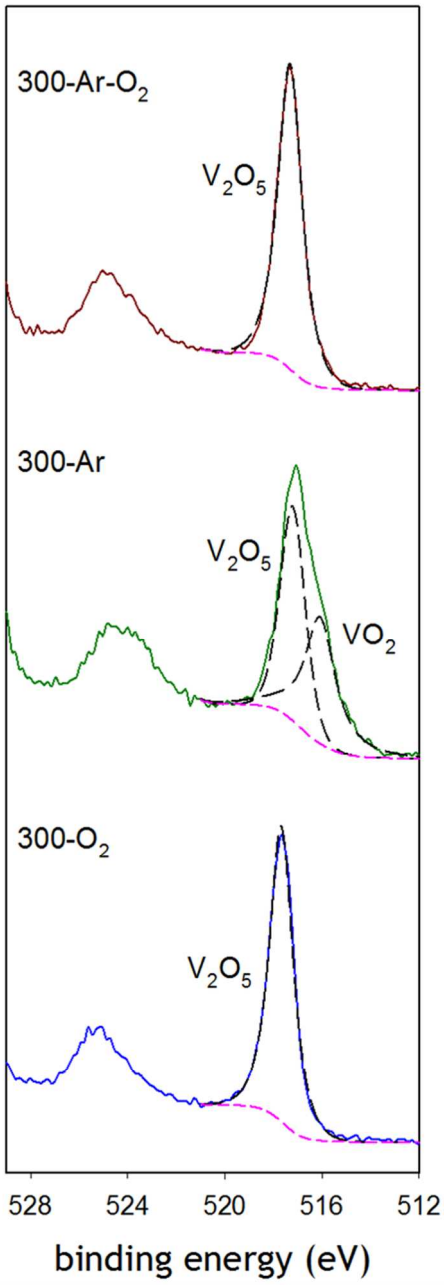

Fig 4 X-ray photoelectron spectra of the V*2p*$_{3/2}$ binding energy for VFe_2Ox aerogels: 300-O_2 (—), 300-Ar (—),300-Ar-O_2 (—), background fit (– – –), and peak fit (– – –).

Figure 5

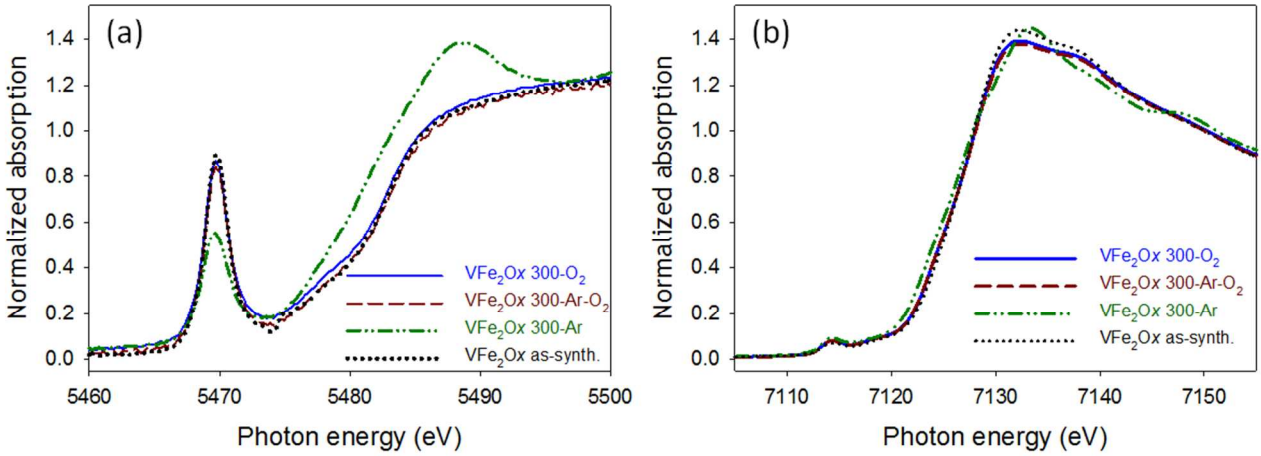

Fig 5 (a) V K-edge and (b) Fe K-edge XANES for VFe_2Ox aerogels: 300-O_2 (—), 300-Ar-O_2 (– – –), 300-Ar (–••–), and as-synthesized (•••).

Figure 6

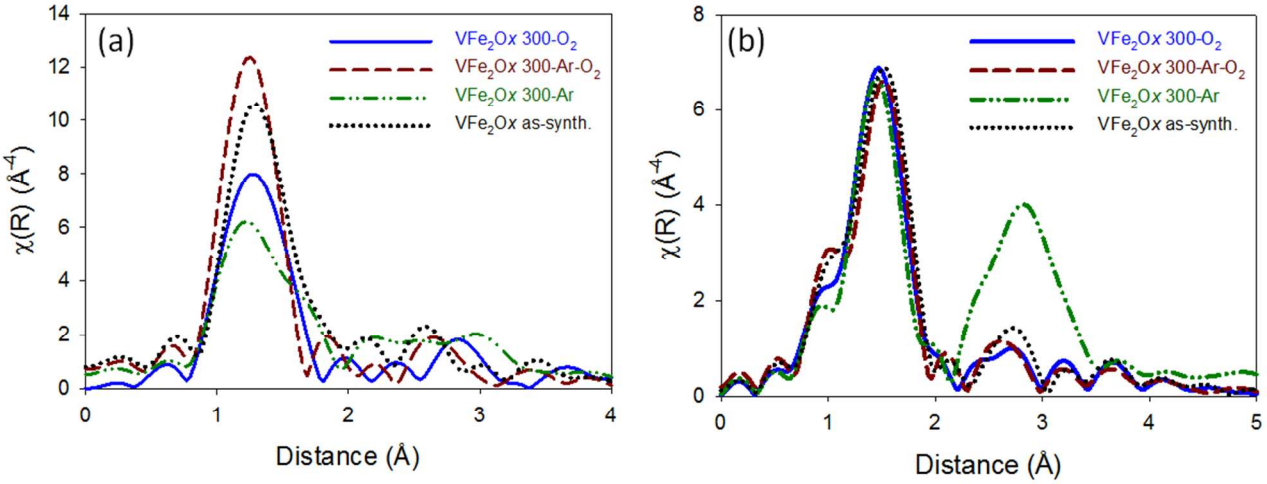

Fig 6 Fourier transform plots of (a) V and (b) Fe K-edge EXAFS spectra for VFe_2Ox aerogels: 300-O_2 (—), 300-Ar-O_2 (– – –), 300-Ar (–••–), and as-synthesized (•••).

Figure 7

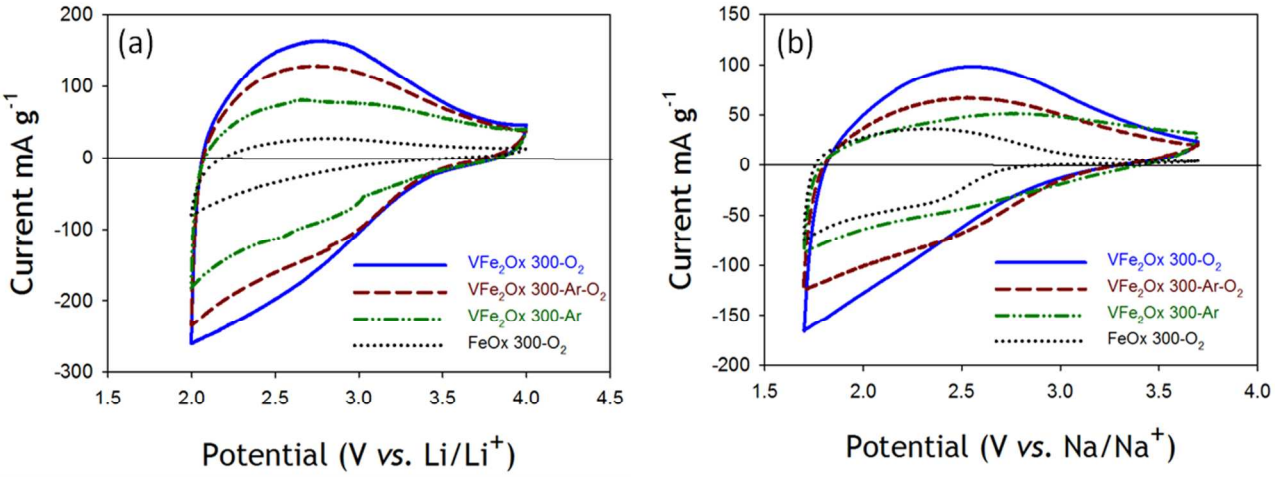

Fig 7 Cyclic voltammograms at 0.5 mV s^{-1} of composite cathodes prepared with (—) VFe_2Ox 300-O_2, (– – –) VFe_2Ox 300-Ar-O_2, (–••–) VFe_2Ox 300-Ar, and (•••) $FeOx$ 300-O_2 in (a) Li^+-containing electrolyte and (b) Na^+-containing electrolyte .

Figure 8

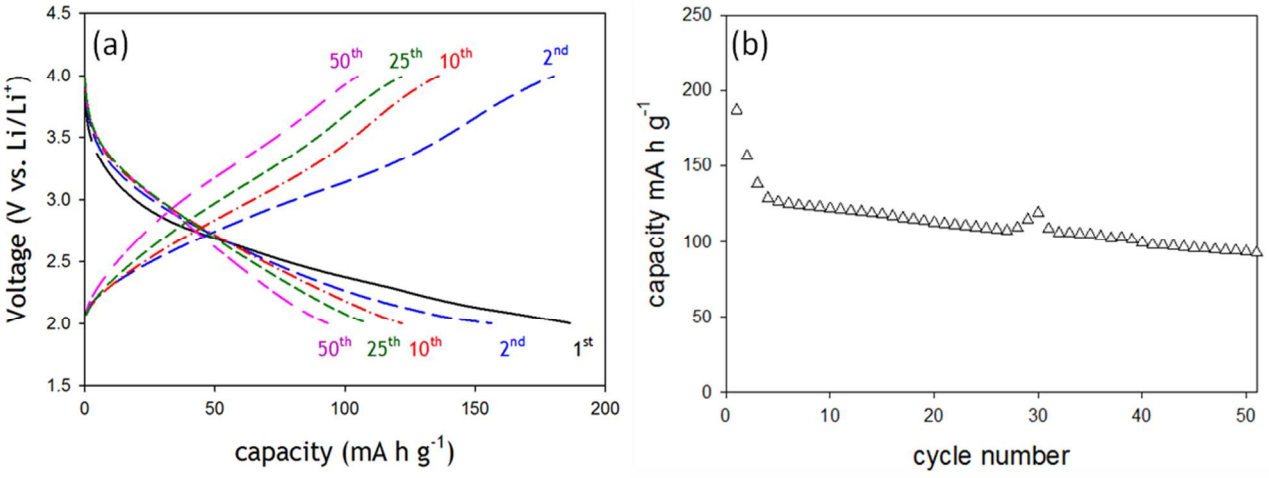

Fig 8 (a) Galvanostatic charge–discharge cycling of a 300-O_2 VFe_2Ox aerogel at 10 mA g^{-1} between 4.0 and 2.0 V *vs.* Li in 1 M $LiPF_6$ in 1/1/1 EC/DEC/DMC; (b) discharge capacity versus cycle number for the galvanostatic cycling.

Notes and references

† Electronic Supplementary Information (ESI) available: See DOI: 10.1039/b000000x/

1 T. Ohzuku and R. J. Brodd, *J. Power Sources*, 2007, **174**, 449–456.
2 M. Pernet, P. Strobel, B. Bonnet, P. Bordet, and Y. Chabre, *Solid-State Ionics*, 1993, **66**, 259–265.
3 S. Kanzaki, T. Inada, T. Matsumura, N. Sonoyama, A. Yamada, M. Takano, and R. Kanno, *J. Power Sources*, 2005, **146**, 323–326.
4 M. Hibino, J. Terashima, and T. Yao, *J. Electrochem. Soc.*, 2007, **154**, A1107–A1111.
5 S. Park, M. Oda, and T. Yao, *Solid-State Ionics*, 2011, **203**, 29–32.
6 L. Bouet, Ph. Tailhades, A. Rousset, B. Domenichini, and B. Gillot, *Solid-State Ionics*, 1993, **52**, 285–286.
7 B. Gillot and V. Nivoix, *Mater. Res. Bull.*, 1999, **34**, 1735–1747 .
8 B. P. Hahn, J. W. Long, A. N. Mansour, K. A. Pettigrew, M. S. Osofsky, and D. R. Rolison, *Energy Environ. Sci.*, 2011, **4**, 1495–1502.
9 J. W. Long, D. R. Rolison, and B. P. Hahn, U.S. Patents 8,388,867; 8,790,612.
10 B. P. Hahn, J. W. Long, and D. R. Rolison, *Acc. Chem. Res.*, 2013, **46**, 1181–1191.
11 B. Koo, H. Xiong, M. D. Slater, V. B. Prakapenka, M. Balasubramanian, P. Podsiadlo, C. S. Johnson, T. Rajh, and E. V. Shevchenko, *Nano Lett.*, 2012, **12**, 2429–2435.
12 B. Koo, S. Chattopadhyay, T. Shibata, V.B. Prakapenka, C.S. Johnson, T. Rajh, and E.V. Shevchenko, *Chem. Mater.*, 2012, **25**, 245–252.
13 D. R. Rolison and B. Dunn, *J. Mater. Chem.*, 2001, **11**, 963.
14 D. B. Le, S. Passerini, J. Guo, J. Ressler, B. B. Owens, and W. H. Smyrl, *J. Electrochem. Soc.*, 1996, **143**, 2099–2104.
15 H. Li, P. He, Y. Wang, E. Hosono, and H. Zhou, *J. Mater. Chem.*, 2011, **21**, 10999–11009.
16 W. Dong, B. Dunn, and D. R. Rolison, *Electrochem. Solid-State Lett.*, 2000, **3**, 457–459.
17 K. E. Swider-Lyons, C. T. Love, and D. R. Rolison, *Solid-State Ionics*, 2002, **152-153**, 99–104.
18 F. Chaput, B. Dunn, P. Fuqua, and K. Salloux, *J. Non-Cryst. Solids*, 1995, **188**, 11–18.
19 S. Passerini, D. B. Le, W. H. Smyrl, M. Berrettoni, R. Tossici, and R. Marassi, *Solid-State Ionics*, 1997, **104**, 195.
20 C. P. Rhodes, W. Dong, J. W. Long, and D. R. Rolison, in *Solid-State Ionics VI*; E. D. Wachsman, K. E. Swider Lyons, M. F. Carolan, F. H. Garzon, M. Liu, J. R. Stetter, Eds.; PV 2002–26, Electrochemical Society: Pennington, NJ, 2003, 478.
21 A. E. Gash, T. M. Tillotson, J. H. Satcher, Jr., J. F. Poco, L. W. Hrubesh, and R. L. Simpson, *Chem. Mater.*, 2001, **13**, 999–1007.
22 J. W. Long, M. S. Logan, C. P. Rhodes, E. E. Carpenter, R. M. Stroud, and D. R. Rolison, *J. Am. Chem. Soc.*, 2004, **126**, 16879–16889.
23 J. W. Long, M. S. Logan, E. E. Carpenter, R. M. Stroud, and D. R. Rolison, *J. Non-Cryst. Solids*, 2004, **350**, 182–188.
24 K. A. Pettigrew, J. W. Long, E. E. Carpenter, C. C. Baker, J. C. Lytle, C. N. Chervin, M. S. Logan, R. M. Stroud, and D. R. Rolison, *ACS Nano*, 2008, **2**, 784–790.
25 S. Célérier, C. Laberty-Robert, J. W. Long, K. A. Pettigrew, R. M. Stroud, D. R. Rolison, F. Ansart, and P. Stevens, *Adv. Mater.*, 2006, **18**, 615–618.
26 A.C. Larson, R.B. Von Dreele, *Los Alamos National Laboratory Report LAUR* 1994, 86-748.
27 B.H. Toby, *J. Apply Crystallogr.* 2001, **34**, 210–213.
28 M. Newville, *J. Synchrotron Rad*., 2001, **8**, 322–324.
29 B. Ravel and M. Newville, *J. Synchrotron Rad.*, 2005, **12**, 537–541.
30 C. N. Chervin, B. J. Clapsaddle, H. W. Chiu, A. E. Gash, J. H. Satcher, Jr., and S. M. Kauzlarich, *Chem. Mater.*, 2008, **18**, 4865–4874.
31 C. N. Chervin, B. J. Clapsaddle, H. W. Chiu, A. E. Gash, J. H. Satcher, Jr., and S. M. Kauzlarich, *Chem. Mater.*, 2006, **18**, 1928–1937.
32 H.-C. Chien, W.-Y. Cheng, Y.-H. Wang, T.-Y. Wei, and S.-Y. Lu, *J. Mater. Chem.*, 2011, **21**, 18180–18182.
33 B. J. Clapsaddle, B. Neumann, A. Wittstock, D.W. Sprehn, A. E. Gash, J. H. Satcher, Jr., R. L. Simpson, and M. Baumer, *J. Sol–Gel Sci. Technol.*, 2012, **64**, 381–389.
34 C. Laberty-Robert, J. W. Long, K. A. Pettigrew, R. M. Stroud, and D. R. Rolison, *Adv. Mater.*, 2007, **19**, 1734–1739.
35 A. E. Gash, J. H. Satcher, Jr., and R. L. Simpson, *Chem. Mater.*, 2003, **15**, 3268–3275.
36 J. Livage, *Chem. Mater.*, 1991, **3**, 578–593.
37 C. N. Chervin, B. J. Clapsaddle, H. W. Chiu, A. E. Gash, J. H. Satcher, Jr., and S. M. Kauzlarich, *Chem. Mater.*, 2005, **17**, 3345–3351.
38 T. Kogure, J. Kameda, and V.A. Dirts, *Clay. Clay Miner.*, 2008, **56**, 612–621.
39 G. Silversmith, D. Depla, H. Poelman, G. B. Marin, and R. De Gryse, *J. Electron. Spectrosc. Relat. Phenom.*, 2004, **135**, 167–175.
40 M. C. Biesinger, B. P. Payne, A. P. Grosvenor, L. W. Lau, A. R. Gerson, and R. St. C. Smart, *Appl. Surf. Sci.*, 2011, **257**, 2717–2730.

41 T. E. Westre, P. Kennepohl, J. G. DeWitt, B. Hedman, K. O. Hodgson, and . I. Solomon, *J. Am. Chem. Soc*., 1997, **119**, 6297-6314.
42 J. Wong, F. W. Lytle, R. P. Messmer, and D. H. Maylotte, *Phys. Rev*., 1984, **B 30(10)**, 5596-5610.
43 A. N. Mansour, P. H. Smith, W. M. Baker, M. Balasubramanian, and J. McBreen, *Electrochim Acta*, 2002, **47**, 3151-3161.
44 M. Nabavi, F. Taulelle, C. Sanchez, and M. Verdaguer, *J. Phys. Chem. Solids*, 1990, **51**, 1375-1382.
45 J. Wong, F.W. Lytle, R. P. Messmer, and D. H. Maylotte, *Phys. Rev.*, 1984, **B30**, 5596–5610.
46 E.E. Carpenter, J.W. Long, D.R. Rolison, M.S. Logan, K.A. Pettigrew, R.M. Stroud, L.T. Kuhn, B.R. Hansen, and S. Morup, *J. Appl. Phys.*, 2006, **99**, 08N711.
47 R. Frison, G. Cernuto, A. Cervellino, O. Zaharko, G.M. Colonna, A. Guagliardi, and N. Masciocchi, *Chem. Mater.*, 2013, **25**, 4820–4827.

VFe_2O_x aerogel architectures are synthesized such that cation-vacancy formation is enhanced by their high surface area and substituting a fraction of the Fe^{3+} sites for high-valent V^{5+}; increased capacity for Li^+- and Na^+-insertion, approaching 130 $mAhg^{-1}$ and 70 $mAhg^{-1}$, respectively, is correlated with a larger concentration of cation vacancies and structural disorder.